


Turning a chiral skyrmion inside out

Vladyslav M. Kuchkin^{1,2} and Nikolai S. Kiselev^{1,*}

¹*Peter Grünberg Institute and Institute for Advanced Simulation, Forschungszentrum Jülich and JARA, 52425 Jülich, Germany*

²*Department of Physics, RWTH Aachen University, 52056 Aachen, Germany*

 (Received 8 December 2019; revised manuscript received 23 January 2020; accepted 23 January 2020; published 10 February 2020)

The stability of two-dimensional chiral skyrmions in a tilted magnetic field is studied. It is shown that by changing the direction and magnitude of the field, one can continuously transform a chiral skyrmion into a skyrmion with opposite polarity and vorticity. This turned inside out skyrmion can be considered as an antiparticle for an ordinary axisymmetric skyrmion. For any tilt angle of the magnetic field, there is a range of its absolute values where two types of skyrmions may coexist. In a tilted field the potentials for interskyrmion interactions are characterized by the presence of local minima suggesting an attractive interaction between the particles. The potentials of interparticle interactions also have so-called fusion channels allowing either the annihilation of two particles or the emergence of a another particle. The presented results are general for a wide class of magnetic crystals with both easy-plane and easy-axis anisotropies.

DOI: [10.1103/PhysRevB.101.064408](https://doi.org/10.1103/PhysRevB.101.064408)

I. INTRODUCTION

Chiral magnetic skyrmions (Sks) are localized magnetic vortices [1], which can be stabilized in materials with a competing Heisenberg exchange and Dzyaloshinskii-Moriya interaction (DMI) [2,3]. A necessary but insufficient condition for the stability of chiral Sks is the presence of a potential energy term, for instance, the interaction with an external magnetic field and/or the magnetocrystalline anisotropy. The latter plays an important role in the case of thin films and multilayer systems [4]. Such systems are typically well described by the two-dimensional (2D) model of a chiral magnet, which is also often utilized for so-called quasi-2D crystals—bulk crystals of particular symmetry allowing DMI between spins contained in specific crystallographic planes, for instance, the lacunar spinel compound GaV₄S₈ [5]. The majority of studies on the stability of chiral Sks [6–12], their interactions, dynamics, and transport properties, have been carried out for the case when the external magnetic field is applied perpendicularly to the plane of the 2D magnet. The number of studies related to the case of a tilted field is limited [13–21]. These publications are mainly related to Sk lattices, their dynamical properties [13–15], and phase transitions [16–21]. The properties of isolated Sks have been partially discussed in Refs. [16,19], where it was shown that in a tilted magnetic field the isolated chiral Sk has an asymmetric magnetic structure, which leads to an anisotropic interskyrmion interaction. It means that the interaction energy between two skyrmions depends on their relative orientation with respect to the in-plane component of the external field. It is worth emphasizing that in both Refs. [16,19] the authors argue that the interaction between Sks remains repulsive. Contrary to this, here we show that in a tilted magnetic field the Sks can attract each other. Besides that, in this paper, we report a number of other fundamentally

new phenomena occurring upon applying a tilted magnetic field to chiral Sks.

II. MODEL

We estimate the stability of Sks by means of a direct energy minimization of the micromagnetic functional [1],

$$\mathcal{E} = \int \left(\mathcal{A} \sum_i (\nabla n_i)^2 + \mathcal{D} w(\mathbf{n}) + U(n_z) \right) t dx dy, \quad (1)$$

where $\mathbf{n} = \mathbf{M}(\mathbf{r})/M_s$ is a continuous unit vector field, M_s is a saturation magnetization, and \mathcal{A} and \mathcal{D} are the micromagnetic constants for isotropic exchange and DMI, respectively. It is assumed that magnetization remains homogeneous along the thickness t . The DMI term $w(\mathbf{n})$ is defined by combinations of Lifshitz invariants,

$$\Lambda_{ij}^{(k)} = n_i \frac{\partial n_j}{\partial r_k} - n_j \frac{\partial n_i}{\partial r_k}.$$

The results presented in this paper are valid for a wide class of chiral magnets of different crystal symmetries with Néel-type modulations [5,22,23] where $w(\mathbf{n}) = \Lambda_{xz}^{(x)} + \Lambda_{yz}^{(y)}$, Bloch-type modulations [24–26] where $w(\mathbf{n}) = \Lambda_{zy}^{(x)} + \Lambda_{xz}^{(y)} + \Lambda_{yx}^{(z)} = \mathbf{n} \cdot (\nabla \times \mathbf{n})$, and D_{2d} symmetry [27] where $w(\mathbf{n}) = \Lambda_{zy}^{(x)} + \Lambda_{xz}^{(y)}$. The last term in (1) represents the potential energy term including uniaxial anisotropy $U_a = K(1 - n_z^2)$ and the Zeeman energy—the interaction with an external magnetic field $U_Z = M_s \mathbf{B} \cdot \mathbf{n}$. The distances, magnetic fields, and energies are given in dimensionless units relative to the equilibrium period of a helical spin spiral [28,29] $L_D = 4\pi \mathcal{A}/|\mathcal{D}|$, the critical field [29] $B_D = \mathcal{D}^2/(2M_s \mathcal{A})$, and the energy of the saturated state $E_0 = 2At$, respectively. The dimensionless magnetic field $\mathbf{h} = \mathbf{B}/B_D$ and anisotropy $u = K/(M_s B_D)$ are two unique control parameters of the system.

For the direct energy minimization of (1) we use a nonlinear conjugate gradient (NCG) method implemented for the NVIDIA CUDA architecture and optimized for the best

*n.kiselev@fz-juelich.de

performance of the advanced numerical scheme ATLAS [30,31]. We use a fourth-order finite-difference scheme on a regular square grid with periodical boundary conditions [31]. The typical size of the simulated domain is $\sim 10L_D \times 10L_D$ with a mesh density Δl given in the number of nodes per L_D , varying from 32 to 1024. Most of the results presented below have been obtained for $\Delta l = 52$. In particular cases, in order to approach the continuum limit, we employ substantially denser meshes with Δl up to 1024 nodes.

III. RESULTS AND DISCUSSION

A. Stability diagram for an isolated chiral skyrmion in a tilted field

We start with the case of a purely isotropic system, $u = 0$. It will be shown below that the discussed phenomena

remain valid for a wide range of positive (easy-axis) and negative (easy-plane) values of the anisotropy. The stability diagram for isolated Sk in a tilted magnetic field, $\mathbf{h} = (h \sin \theta_h, 0, h \cos \theta_h)$, is shown in Fig. 1(a). For any tilt angle $0 \leq \theta_h \leq \pi$, the range of absolute values of the external field h , in which isolated Sk remains stable, is bounded by an elliptical instability field h^e from below and by a collapse or blowup field h^c from above. Below the elliptical instability field $h < h^e$, the solution for isolated Sk becomes unstable with respect to an elliptical deformation which results in the transformation of the Sk into an isolated spiral strip [7]. On the other hand, approaching the collapse field the Sk gradually shrinks and disappears for $h > h^c$.

The critical fields $h^e(\theta_h)$ and $h^c(\theta_h)$ exhibit a quite different dependence on the mesh density used in numerical energy minimization schemes. The value of the elliptical

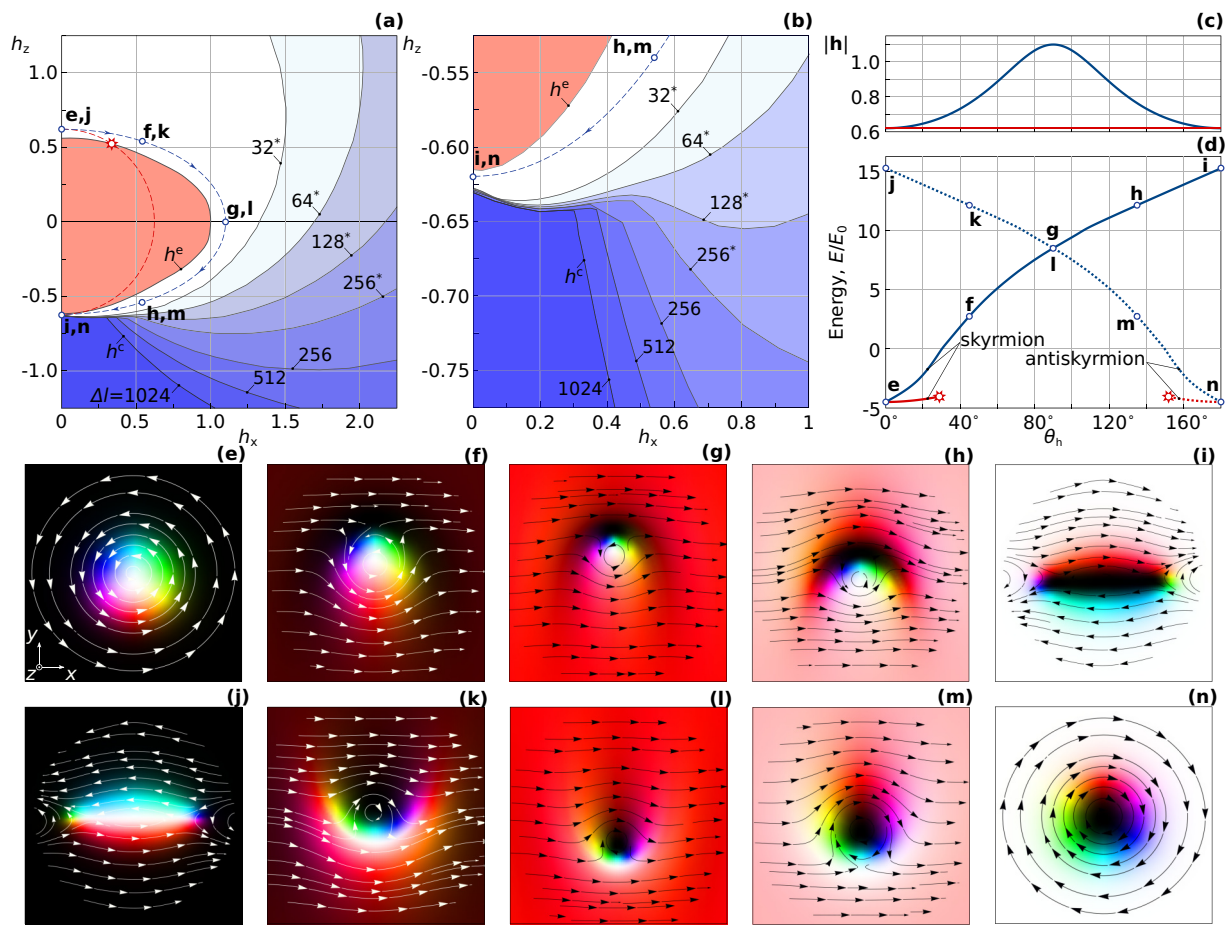


FIG. 1. (a), (b) Stability diagram for an isolated skyrmion in a tilted magnetic field $\mathbf{h} = (h_x, 0, h_z)$ at $u = 0$. h^e and h^c are the critical fields corresponding to the elliptical instability and the collapse of isolated skyrmion, respectively. With increasing mesh density Δl the region for skyrmion stability extends. For Δl values marked with an asterisk, see the main text. The dashed red line in (a) corresponds to the case when $|\mathbf{h}| = 0.62$ and does not change with the tilt angle θ_h [see the red line in (c)]. This leads to skyrmion instability at the point marked by a star symbol in (a) and (d). The dashed blue line in (a) and (b) is the path along which the value of $|\mathbf{h}|$ changes with θ_h [see the blue line in (c)]. At any point (h_x, h_z) along this path there are two stable skyrmion solutions with opposite topological charge Q . The energies of both solutions as functions of θ_h are given in (d). Blue lines: Solid line for $Q = -1$, dotted line for $Q = +1$. The red lines in (d) correspond to the fixed $|\mathbf{h}| = 0.62$. The spin textures in (e)–(i) and (j)–(n) represent the transient states of two skyrmion solutions with $Q = -1$ and $Q = 1$, respectively. The images in each row from left to right correspond to $\theta_h = 0, \pi/4, \pi/2, 3\pi/4$, and π , respectively. In (e)–(n) the standard color code scheme [31] is used: Black and white correspond to up and down spins, respectively, and red-green-blue is defined by the azimuthal angle with respect to the x axis; the lines and arrows in (e)–(n) denote the streamlines of the in-plane component of the magnetization [32]. For the spin texture, see also Fig. 4 in Appendix A.

instability field $h^c(\theta_h)$ converges quickly with an increase of the mesh density. It does not change significantly for $\Delta l \gtrsim 64$. Note, the curve h^c in Fig. 1(a) is not fully symmetric with respect to the horizontal axis $h_z = 0$. For instance, in the case of a perpendicular field, $h_z^c = 0.52$ and -0.62 for the magnetic field pointing along the positive direction of z axis, $\mathbf{h} \uparrow \uparrow \hat{\mathbf{e}}_z$, and in the opposite direction, $\mathbf{h} \downarrow \downarrow \hat{\mathbf{e}}_z$, respectively.

In contrast to h^c , the collapse field h^c does not converge when approaching the continuum limit ($\Delta l \rightarrow \infty$) as shown in Fig. 1(a) for different Δl values. The behavior of the numerical solutions observed here is in line with the results of Ref. [12], where it is proven that in the micromagnetic limit, for the particular case of $\theta_h = 0$ and $u = 0$, the stability of the skyrmion solution is not bounded from above, even for $h \rightarrow \infty$. Following the approach of Ref. [12], we prove that

the above statement can be rigorously extended for the tilt angles, at least in the range $0 \leq \theta_h < \pi/3$ (see Appendix B).

Remarkably, even for a fully reversed field, $h_x = 0$ and $h_z < 0$, there is a finite range window where the Sk solution remains stable [see Fig. 1(b)]. A continuous transition between the equilibrium Sk solutions shown in Figs. 1(e) and 1(i) can be achieved by varying the absolute value and the tilt angle of the magnetic field, such that $h^c(\theta_h) < |\mathbf{h}| < h^c(\theta_h)$ [see Fig. 1(c) and the corresponding dashed blue line in Figs. 1(a) and 1(b)].

Because of the continuity of such transitions and the fact that the states in Figs. 1(e) and 1(i) have an opposite sign of both polarity and vorticity [33], one may conclude that the topological charge of these states as well as for all transient states in Figs. 1(f)–1(h) is identical. It is also easy to show that for all spin textures in Figs. 1(e)–1(h) the topological charge

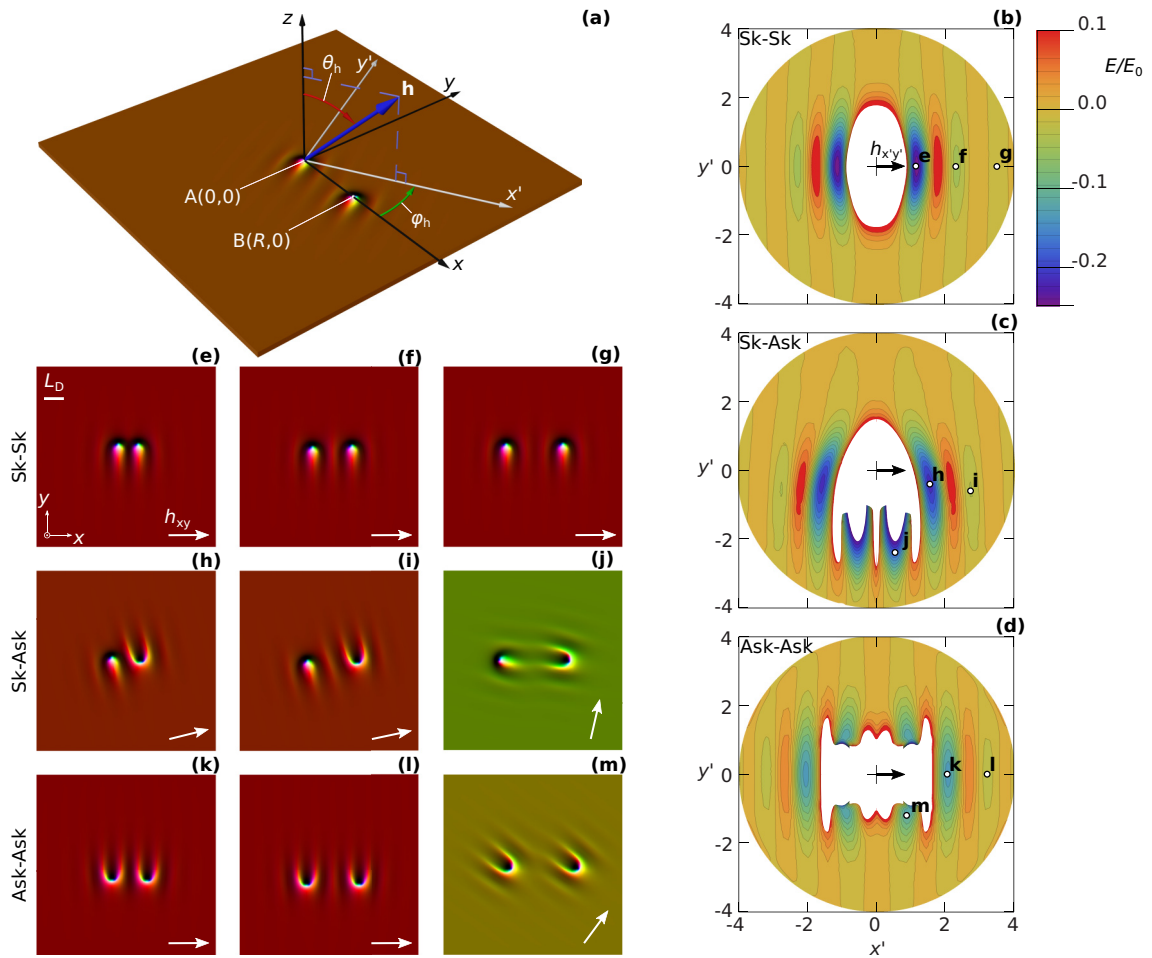


FIG. 2. (a) Simulated domain of 1024×1024 lattice sites. The points A and B are the positions of two pinned spins with $\mathbf{n} = (0, 0, -1)$ at the center of two interacting skyrmions. (b)–(d) are the potential energies of two interacting particles calculated for $\theta_h = \pi/3$, $|\mathbf{h}| = 0.8$ ($u = 0$ and $\Delta l = 52$), and given in the local coordinate frame $(x', y') = (R \cos \phi_h, -R \sin \phi_h)$, in which the in-plane component of the field is always pointing along the x' axis. The distances x' and y' are given in units of L_D . (b)–(d) correspond to skyrmion-skyrmion, skyrmion-antiskyrmion, and antiskyrmion-antiskyrmion interactions, respectively. The spin textures in (e)–(i), (k), and (l) illustrate equilibrium states obtained by energy minimization without the spins being pinned. These states correspond to the local energy minima marked accordingly in (b)–(d). The spin textures in (j) and (m) were obtained with pinned spins and illustrate the states that are precursory for the fusion of two particles. All images in (e)–(m) have an identical size and show only the central part of the simulated domain. The white arrows in the bottom left corner indicate the direction of the in-plane component of the applied magnetic field h_{xy} .

defined by the invariant $Q = 1/(4\pi) \int [\mathbf{n} \cdot (\partial_x \mathbf{n} \times \partial_y \mathbf{n})] dx dy$ equals -1 .

The symmetry of the problem permits us to apply the same analysis to an equivalent solution, which at magnetic field \mathbf{h} opposite to \hat{e}_z , $\mathbf{h} \downarrow \uparrow \hat{e}_z$ represents an axially symmetric Sk with opposite polarity [see Fig. 1(n)]. The topological charge for the Sk in Fig. 1(n), as well as for all other states in Figs. 1(j)–1(m), is $Q = +1$. Thereby, the Sk with $Q = -1$ and the antiskyrmion (ASk) with $Q = +1$ may coexist at any tilt angle. Moreover, the energies of Sk and ASk become equal when $\theta_h = \pi/2$ [see Fig. 1(d)].

The stability of Sk and ASk in a tilted field can be also reproduced in the corresponding spin-lattice model. Note that the h^c curves in Figs. 1(a) and 1(b) for $\Delta l = 32, 64, 128$, and 256 marked with an asterisk have been calculated with the nearest-neighbor spin-lattice model, where Δl has the meaning of the number of lattice sites per L_D (see Appendix A).

B. Interskyrmion interactions

The interactions between Skys in a tilted field are fundamentally different from those of axisymmetric Skys in a perpendicular field because of the broken symmetry of their spin texture. For the calculation of the potentials of the interskyrmion interactions presented in Figs. 2(b)–2(d), we performed the energy minimization on a large size domain with two pinned spins at the centers of the two Skys, as depicted in Fig. 2(a). The white region in the center of the energy profiles is defined by critical distances, where the interaction energy is either too high or too low. This is attributed to the distortion of the Skys' spin texture. The calculation of the interaction energies with pinned spins at such small distances has no physical meaning.

The common features of the potentials corresponding to the different pairs of interacting particles in Figs. 2(b)–2(d) are as follows: (i) For any fixed $\varphi_h \neq \pm\pi/2$ the interaction energy between particles oscillates in strength and sign with the distance from negative (attraction) to positive (repulsion); and (ii) for any pair of particles there are a few local minima corresponding to stable configurations. In fact, we believe that for any $\theta_h > 0$, there are an infinite number of such minima, while their depths as well as the energy barrier between them get smaller as the distance increases. The local minima also disappear when $\theta_h \rightarrow 0$ or π [16]. The ASk interaction reveals two remarkable features: an asymmetry of the Sk-ASK potential and the presence of so-called fusion channels. The latter means that there are specific mutual orientations of the particles leading them to fuse [see Figs. 2(j) and 2(m)]. Note, this fusion occurs with the conservation of the topological charge, and leads either to the annihilation of the interacting particles or to the emergence of a another particle. The processes of Sk-ASK and ASk-ASK fusion are presented in the video files in the Supplemental Material [34].

The fusion channels are always present on the interaction energy profile involving ASk, even in the perpendicular field. The latter can be proven via the analysis of the asymptotic behavior of analytical Sk solutions (see Appendix C). The coexistence of Sk and ASk and their ability for fusion disputes the statements postulated in earlier works [35–38]. For instance, in Ref. [35] the authors argued the following: “Nor is it

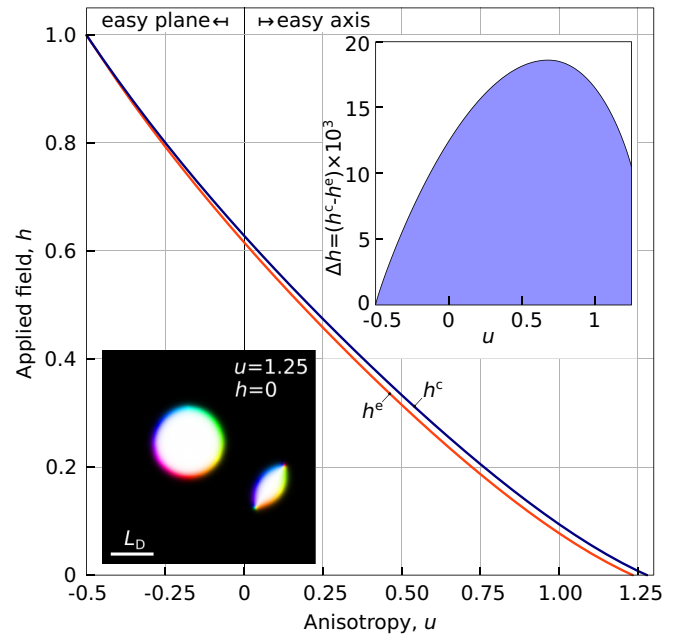


FIG. 3. The range of existence for an antiskyrmion in a perpendicular magnetic field, $\mathbf{h} = (0, 0, h)$, is bounded by the fields of elliptic instability h^e and collapse h^c . The field range Δh (right top inset) converges to zero at the Bogomol’nyi point [39], $u = -0.5$ and $h = 1$. The bottom left inset illustrates the coexistence of Sk and ASk without fusion at large distances for the case of strong perpendicular anisotropy and zero field.

possible to fuse a skyrmion with an antiskyrmion to annihilate them since the system under consideration consists only of one species of skyrmions.” The statement of the uniqueness of the Sk solution has been disproved in Ref. [31]. Here, we demonstrate the possibility of Sk and ASk fusion.

C. The case of nonzero anisotropy

The stability of Skys in the whole range of magnetic field tilt angles can be observed not only for isotropic chiral magnets but also for easy-plane and easy-axis anisotropies. The criterion for this is the stability of the ASk in the perpendicular field. The diagram in Fig. 3 illustrates a wide range of positive and negative values of u where ASk remains stable. Note, the critical point $h = 1$, $u = -0.5$ corresponds to the so-called Bogomol’nyi point [39], where a large set of skyrmion solutions can be found analytically. This also includes the solution for ASk presented here. With increasing u , both h^e and h^c decrease gradually and for a strong enough uniaxial anisotropy, the stability of Sk and ASk can be achieved even in zero magnetic field (see the inset in Fig. 3).

One has to make an important remark regarding previous works reporting the stability of the in-plane Skys similar to those in Figs. 1(g) and 1(i) even at $h = 0$ (see Refs. [40–42]). The value of the easy-plane anisotropy used in these works corresponds to $u \lesssim -2$, which is far below the critical value of $u = -0.5$. Indeed, to a certain extent, such solutions can be treated as Skys, although, de facto, they share more similarity to pairs of vortices and antivortices. In Appendix D we provide simple arguments that support this statement. In particular,

we show that for the case of strong easy-plane anisotropy $u \ll -0.5$ and zero external field $\mathbf{h} = 0$, there are four types of stable vortex solutions depicted in Fig. 6. These vortices are distinguished by the sign of the vorticity and polarity of the vortex core. The topological charge of the vortices is fractional, $Q = \pm 1/2$. We provide a few examples (see Fig. 7) which illustrate some complex multivortex configurations with integer and fractional values of Q . In this regard, it seems reasonable to use precisely these four vortices as unique countable objects that describe the state of the system.

IV. CONCLUSIONS

In conclusion, in this paper, we investigate the stability of 2D chiral magnetic skyrmions in the presence of a tilted magnetic field. It is shown that by changing the absolute value of the magnetic field with the tilt angle one can *continuously* transform the axisymmetric skyrmion at $\mathbf{h} \uparrow \uparrow \hat{\mathbf{e}}_z$ (or $\mathbf{h} \downarrow \downarrow \hat{\mathbf{e}}_z$) into a nonaxisymmetric skyrmion with opposite polarity and opposite vorticity which remains stable even in a fully inverted field $\mathbf{h} \downarrow \downarrow \hat{\mathbf{e}}_z$ ($\mathbf{h} \uparrow \uparrow \hat{\mathbf{e}}_z$). In other words, one can turn a chiral skyrmion inside out. It is shown that in the tilted magnetic field, the interaction potentials of the chiral skyrmions, which are characterized by several local minima, reveal an attractive interaction between the particles. These interactions can be controlled by the strength and tilt angle of the external magnetic field. Complex potentials of interskyrmion interactions allow not only the formation of various skyrmion clusters but also a fusion of the skyrmions. The discussed phenomena are general and applicable for a wide class of crystals with trigonal, tetragonal, and cubic symmetry.

ACKNOWLEDGMENTS

The authors thank Filipp Rybakov, Juba Bouaziz, and Stefan Blügel for fruitful discussions. The authors also thank Filipp Rybakov for providing the software for micromagnetic simulations and Deutsche Forschungsgemeinschaft (DFG) for support through SPP 2137 ‘‘Skyrmionics’’ Grant No. KI 2078/1-1.

APPENDIX A: SPIN-LATTICE MODEL

The results presented in the main text are based on an analysis of a micromagnetic model but remain valid also for the spin-lattice model,

$$E = -J \sum_{\langle ij \rangle} \mathbf{n}_i \cdot \mathbf{n}_j - \sum_{\langle ij \rangle} \mathbf{D}_{ij} \cdot [\mathbf{n}_i \times \mathbf{n}_j] - K \sum_i n_{z,i}^2 - \mu_s \mathbf{B}_{\text{ext}} \cdot \sum_i \mathbf{n}_i, \quad (\text{A1})$$

where $\mathbf{n}_i = \mu_i / \mu_s$ is the unit vector of the magnetic moment at lattice site i , $\langle ij \rangle$ denotes the summation over all nearest-neighbor pairs, J is the Heisenberg exchange constant, and \mathbf{D}_{ij} is the Dzyaloshinskii-Moriya vector defined as $\mathbf{D}_{ij} = D \mathbf{r}_{ij}$ with the scalar constant D and the unit vector \mathbf{r}_{ij} pointing from site i to site j , K is an uniaxial anisotropy constant, and \mathbf{B}_{ext} is an external magnetic field.

The equilibrium period of the spin spiral in model (A1) at zero magnetic field has an exact solution [43],

$$L_D^* = 2\pi a / \arctan(D/J). \quad (\text{A2})$$

For weak DMI, $D \ll J$, it can be approximated with the exact solution of a spin spiral period in a continuum model,

$$L_D^* \approx L_D = 2\pi a J / D. \quad (\text{A3})$$

In Fig. 4 we show the spin texture of skyrmions corresponding to the case of a perpendicular field. It is worth emphasizing that in a fully isotropic micromagnetic model the energy of axially nonsymmetric skyrmions [Figs. 1(i) and 1(j)] does not depend on how the semi-axes of such an elliptical object are oriented with respect to the x and y axis. In contrast to this, in the spin-lattice model, there is a significant contribution of anisotropy induced by a natural discretization of the system [44]. A clear manifestation of this effect is that the elliptical shaped skyrmion has the lowest energy only when its semi-axes coincide with the diagonals of a square lattice as in Figs. 4(b) and 4(d).

APPENDIX B: ENERGY UPPER BOUND FOR SKYRMION IN A TILTED MAGNETIC FIELD

To estimate the stability of a chiral skyrmion in a tilted magnetic field we follow the approach of Ref. [12]. In particular, without loss of generality, the functional (1) of the main text can be written in the following reduced form,

$$\begin{aligned} \mathcal{E}(\mathbf{n}) &= \mathcal{E}_{\text{ex}}(\mathbf{n}) + \mathcal{E}_{\text{DMI}}(\mathbf{n}) + \mathcal{E}_Z(\mathbf{n}) \\ &= \iint \left[\frac{1}{2} (\nabla \mathbf{n})^2 + 2\epsilon \left(n_x \frac{\partial n_z}{\partial y} - n_y \frac{\partial n_z}{\partial x} \right) + \frac{\epsilon}{4} |\mathbf{n} - \mathbf{e}_z|^2 \right] dx dy, \end{aligned} \quad (\text{B1})$$

where $\epsilon = 1/(2h)$. We consider an axially symmetric ansatz for the skyrmion solution [12]. Next, we model a skyrmion profile in a tilted field by applying a rotation matrix about the y axis to all spins,

$$\mathbf{n} = \begin{pmatrix} \cos \theta_h & 0 & \sin \theta_h \\ 0 & 1 & 0 \\ -\sin \theta_h & 0 & \cos \theta_h \end{pmatrix} \begin{pmatrix} -f'_R(r) \sin \phi \\ f'_R(r) \cos \phi \\ \text{sgn}(r-1) \sqrt{1 - [f'_R(r)]^2} \end{pmatrix}, \quad (\text{B2})$$

where the function f_R is defined as

$$f_R(r) = \begin{cases} \ln(1 + r^2), & \text{for } 0 \leq r \leq R, \\ c, & \text{for } r \geq 2R, \end{cases} \quad (\text{B3})$$

where c is a positive constant. The following conditions are applied to the first and second derivatives of the function f_R ,

$$0 \leq f'_R(r) \leq \frac{2r}{1+r^2}, \quad 0 \leq -f''_R(r) \leq \frac{c}{1+r^2}, \quad \text{for } r \geq R \gg 1. \quad (\text{B4})$$

The advantage of such an ansatz is that it describes the near-core asymptotic behavior of an exact skyrmion solution.

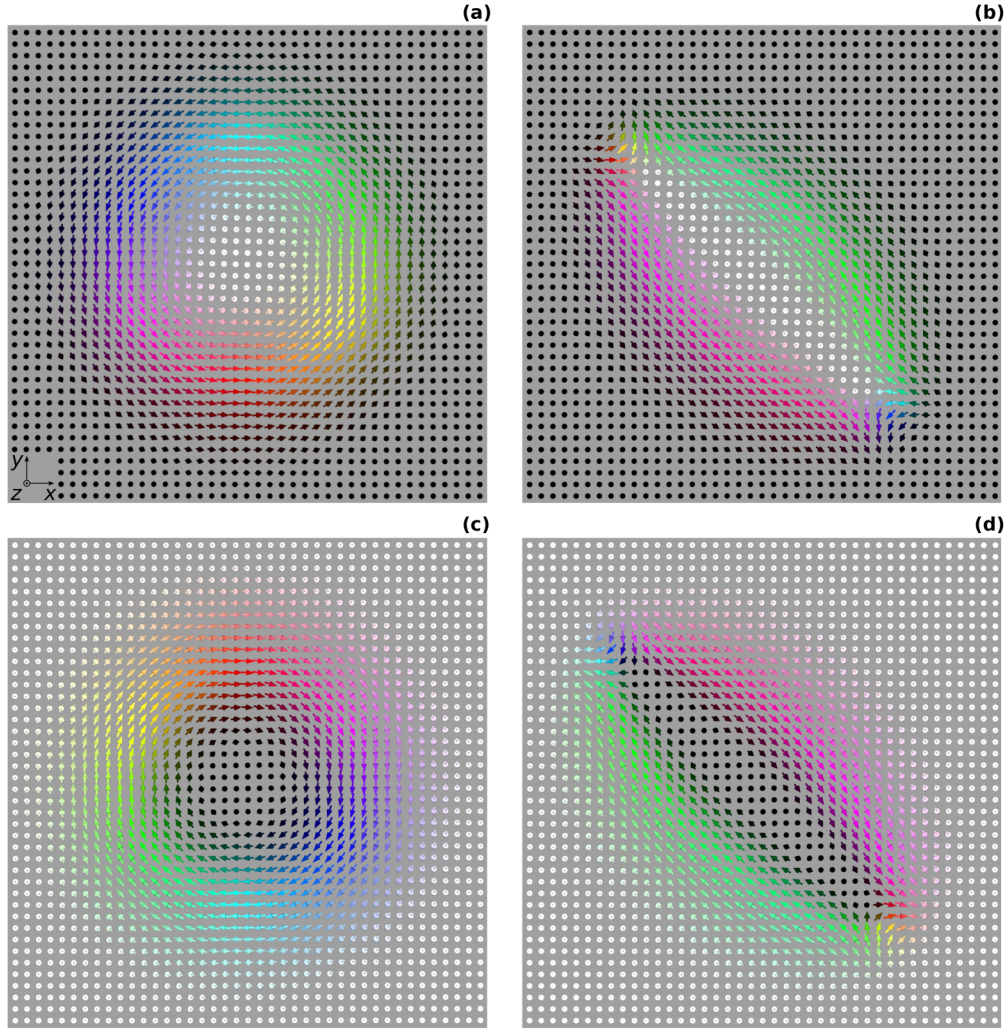


FIG. 4. Equilibrium spin texture of skyrmions with different polarity p and vorticity v calculated for the spin-lattice model (A1) with the following parameters: $J = 1$, $|D| = 0.1963$, $K = 0$, and $\mu_s B_{\text{ext}} = 0.024$ which correspond to $L_D \approx 32$ ($L_D^* \approx 32.4$), $u = 0$, $h \approx 0.623$. The skyrmion in (a) has $p = -1$, $v = 1$, and topological charge $Q = -1$, in (b) $p = -1$, $v = -1$, $Q = +1$, in (c) $p = +1$, $v = 1$, $Q = 1$, and in (d) $p = 1$, $v = -1$, $Q = -1$. The energy minimization has been performed on a square domain of 80×80 lattice sites. We use the same color code for spin directions as in the main text. The black spins are pointed towards the viewer and white spins in the opposite direction.

In the case of the high magnetic field, $\epsilon \ll 1$, the exchange and Zeeman energy terms are bounded from above,

$$\mathcal{E}_{\text{ex}}(\mathbf{n}) + \mathcal{E}_Z(\mathbf{n}) \leq 4\pi + \pi\epsilon \ln(1 + R^2) + c \left(\frac{1}{R^2} + \epsilon \right). \quad (\text{B5})$$

Now let us estimate the bounding energy of DMI. In the region $r \leq R$, the DMI energy is

$$\mathcal{E}_{\text{DMI}}^*(\mathbf{n}) = -8\pi\epsilon \frac{R^2(1 + (R^2 - 1)\cos\theta_h)\cos^2(\theta_h/2)}{(1 + R^2)^2}. \quad (\text{B6})$$

In the region $R < r \leq 2R$ the DMI energy density is

$$\mathcal{E}_{\text{DMI}}^{**}(\mathbf{n}) = 2\pi\epsilon \int_R^{2R} \frac{\sin^2\theta_h f'(1 - f^2) + r(\sin^2\theta_h + f^2(\cos\theta_h + \cos 2\theta_h))f''}{\sqrt{1 - f^2}} dr \leq \int_R^{2R} \frac{2\pi\epsilon r \sin^2\theta_h}{1 + r^2} dr, \quad (\text{B7})$$

at least when $\cos\theta_h + \cos 2\theta_h \geq 0$, meaning $\theta_h \leq \pi/3$. Taking into account (B6) and (B7), the upper bound DMI energy $\mathcal{E}_{\text{DMI}} = \mathcal{E}_{\text{DMI}}^* + \mathcal{E}_{\text{DMI}}^{**}$ is

$$\mathcal{E}_{\text{DMI}}(\mathbf{n}) \leq -8\pi\epsilon \frac{R^2(1 + (R^2 - 1)\cos\theta_h)\cos^2(\theta_h/2)}{(1 + R^2)^2} + 2\pi\epsilon \sin^2\theta_h \ln \frac{1 + 4R^2}{1 + R^2}. \quad (\text{B8})$$

Defining $\tilde{\mathbf{n}} = \mathbf{n}(\lambda r)$, where λ is the rescaling parameter, we get for the total energy of our ansatz solution,

$$\begin{aligned} \mathcal{E}(\tilde{\mathbf{n}}) \leq & 4\pi + \frac{\pi\epsilon}{\lambda^2} \ln(1 + R^2) + c \left(\frac{1}{R^2} + \frac{\epsilon}{\lambda^2} \right) \\ & - \frac{8\pi\epsilon R^2(1 + (R^2 - 1) \cos \vartheta_h) \cos^2 \frac{\vartheta_h}{2}}{\lambda (1 + R^2)^2} \\ & + \frac{2\pi\epsilon \sin^2 \vartheta_h}{\lambda} \ln \frac{1 + 4R^2}{1 + R^2}. \end{aligned} \quad (\text{B9})$$

Now choosing $R = \frac{|\ln \epsilon|}{\sqrt{\epsilon}}$ and $\lambda = L |\ln \epsilon|$, one can write the following inequality for the total energy,

$$\begin{aligned} \mathcal{E}(\tilde{\mathbf{n}}) \leq & 4\pi + \frac{\epsilon}{|\ln \epsilon|} \left(-\frac{8\pi}{L} \cos \theta_h \cos^2(\theta_h/2) + \frac{\pi}{L^2} \right. \\ & \left. + \frac{2\pi(\ln 4) \sin^2 \theta_h}{L} + O(1) \right), \end{aligned} \quad (\text{B10})$$

and minimizing this expression with respect to $L > 0$ gives

$$L = \left(4 \cos \theta_h \cos^2 \frac{\theta_h}{2} - (\ln 4) \sin^2 \theta_h \right)^{-1}. \quad (\text{B11})$$

Note that L in (B11) remains positive only for angle $\theta_h \leq \pi/3$. This critical angle defines the limit of our ansatz (B2). Thereby, the energy of a skyrmion in an external magnetic field tilted by the angle $0 \leq \theta_h \leq \pi/3$ with respect to the plane normal is bounded, at least, by the value

$$\begin{aligned} \mathcal{E}(\tilde{\mathbf{n}}) \leq & 4\pi + \frac{\epsilon\pi}{|\ln \epsilon|} \\ & \times \left[-\left(4 \cos \theta_h \cos^2 \frac{\theta_h}{2} - (\ln 4) \sin^2 \theta_h \right)^2 + O(1) \right]. \end{aligned} \quad (\text{B12})$$

It means that the energy of an approximate skyrmion solution is lower than the energy of the Belyavin-Polyakov soliton (4π). Thereby, the exact skyrmion solution is also less than 4π even when $h \rightarrow \infty$ ($\epsilon \rightarrow 0$).

With the simplified ansatz (B2) and (B3) which does not take into account an asymmetry of the skyrmion in the tilted magnetic field, the above remains true only for $\theta_h \leq 60^\circ$. Nevertheless, there is no doubt that by using a more advanced ansatz one will be able to obtain a higher value of the critical angle which will even better correlate with the results of the numerical calculations presented in the main text.

APPENDIX C: ANALYSIS OF SKYRMION AND ANTISKYRMION ASYMPTOTICS

To analyze the asymptotic behavior of the skyrmion and antiskyrmion solutions we solve the variational problem for the micromagnetic functional (1) in the main text, where the vector field $\mathbf{n}(x, y)$ is defined by the spherical coordinates Θ, Φ ,

$$\mathbf{n} = \begin{pmatrix} \cos \theta_h \sin \Theta \cos \Phi + \sin \theta_h \cos \Theta \\ \sin \Theta \sin \Phi \\ -\sin \theta_h \sin \Theta \cos \Phi + \cos \theta_h \cos \Theta \end{pmatrix}. \quad (\text{C1})$$

The Euler-Lagrange equations for the functional (1) for radially symmetric solutions is

$$\begin{aligned} \Delta \Theta + 4\pi \sin \Theta (\mathbf{n} \cdot \nabla \Phi - \pi h) - \frac{1}{2} \sin 2\Theta (\nabla \Phi)^2 &= 0, \\ \Delta \Phi \sin^2 \Theta - 4\pi \mathbf{n} \cdot \nabla \Theta \sin \Theta \\ &+ \left(\nabla \Theta \cdot \nabla \Phi - 2\pi \sin \theta_h \frac{\partial \Theta}{\partial x} \right) \sin 2\Theta = 0. \end{aligned} \quad (\text{C2})$$

We assume that the boundary conditions obey $\Theta(0, 0) = \pi$, $\Theta(x, \pm\infty) = \Theta(\pm\infty, y) = 0$. The asymptotic behavior of the skyrmion solutions of Eq. (C2) for $r = \sqrt{x^2 + y^2} \rightarrow \infty$ can be written as follows,

$$\Theta = c^2/\sqrt{r} \cdot e^{-2\pi\sqrt{h-\sin^2\theta_h}r}, \quad (\text{C3})$$

$$\Phi = \pm(\phi + \pi/2) + 2\pi r \sin \theta_h \cos \phi + \mathcal{F}(\phi), \quad (\text{C4})$$

where the plus and minus sign stand for skyrmion and antiskyrmion solutions, respectively, c is an arbitrary constant, $\mathcal{F}(\phi)$ some 2π -periodic function, and r and $\phi = \arctan(y/x)$ are the radial and angular coordinates in a polar coordinate system, respectively. In the case of a perpendicular field, $\theta_h = 0$, the asymptotic for the skyrmion takes a simplified form [45,46],

$$\begin{aligned} \Theta &= c^2/\sqrt{r} \cdot e^{-2\pi\sqrt{h}r}, \\ \Phi &= \phi + \pi/2, \end{aligned} \quad (\text{C5})$$

and for an antiskyrmion,

$$\begin{aligned} \Theta &= c^2/\sqrt{r} \cdot e^{-2\pi\sqrt{h}r}, \\ \Phi &= -\phi - \pi/2 + \mathcal{F}(\phi). \end{aligned} \quad (\text{C6})$$

In a linear approximation of adding spin waves we get the potential of the interaction between skyrmions and antiskyrmions, which equals the energy density of (1) at the middle point between the particles [see the star symbol in Fig. 5(a)]. The skyrmion-antiskyrmion and antiskyrmion-antiskyrmion interaction potentials in a perpendicular applied magnetic field are shown on Figs. 5(b) and 5(c). In the case of $\theta_h \neq 0$, the interaction energy demonstrates oscillatory behavior and direct use of the method above is impossible.

APPENDIX D: SKYRMIONLIKE STATES COMPOSED OF VORTICES AND ANTIVORTICES; THE CASE OF STRONG EASY-PLANE ANISOTROPY

In the case of strong easy-plane anisotropy, $u \ll 0$, the energy minimization of the states composed of skyrmions or antiskyrmions leads to an appearance of textures which are morphologically very similar to those discussed in the main text [compare the states in Figs. 6(a) and 6(c) to the states depicted in Figs. 1(g) and 1(l)]. Such states can be stabilized in the system even without applying an external field [40–42]. Similar to skyrmions these states may have a positive or negative topological charge and exhibit particlelike properties, meaning that they can move and interact with each other [40–42]. In particular, at small distances the states shown in Figs. 6(a) and 6(c) attract each other, which in turn leads to their annihilation. Moreover, the particles with identical

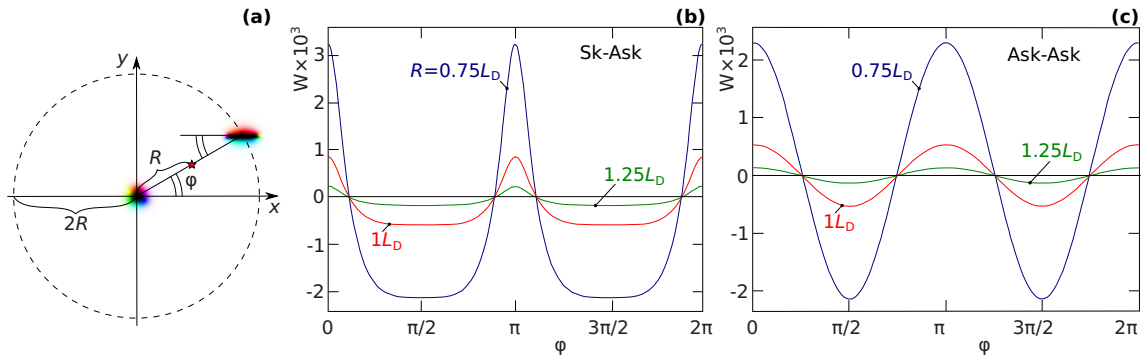


FIG. 5. (a) Schematic representation of two interacting particles (skymion and antiskymion) at a distance $2R$ in the perpendicular magnetic field, $\mathbf{h} = (0, 0, 0.62)$, $u = 0$. The mutual orientation of the particles is defined by the azimuthal angle φ . (b) and (c) are the potential W 's calculated at the middle point between particles [star symbol in (a)] as functions of angle φ , for a skymion-antiskymion in (b) and an antiskymion-antiskymion in (c). Note, $W < 0$ and $W > 0$ correspond to repulsion and attraction, respectively.

topological charge attract each other and may form clusters mainly in the form of chains of particles. These two facts, indeed, show a lot of similarity between the objects stabilized at strong easy-plane anisotropy and skymions in a tilted field. On the other hand, there are strong arguments supporting the statement that these objects possess more similarities to vortex and antivortex pairs rather than skymions.

Below we show examples of different textures appearing in the case of strong easy-plane anisotropy. These representative textures were obtained by direct energy minimization for the functional (1) with $|\mathbf{h}| = 0$, $u = -2$, and discretization $\delta l = 52$. For comparison, the micromagnetic parameters used in previous works reporting the study of so-called *in-plane*

skymions correspond to the following anisotropy: $u = -1.96$ [40], $u = -2.00$ [41], and in Ref. [42] for a different set of parameters $u = -2.88$, -3.33 , and -4.67 .

First of all, it is easy to show that the states in Figs. 6(a) and 6(c) can be decomposed into stable isolated states. Indeed, Figs. 6(e)–6(h) illustrate two types of vortices and antivortices with a different polarity of the cores. It is well known that an isolated vortex cannot be stabilized in an infinite sample (or in the domain with periodical boundary conditions) and only a vortex and antivortex pair can do that. Because of that, in order to visualize such stable isolated vortices in Figs. 6(e)–6(h), we use a finite-size domain with open boundary conditions. It is easy to see that the state in Fig. 6(b) [Fig. 6(d)] can be

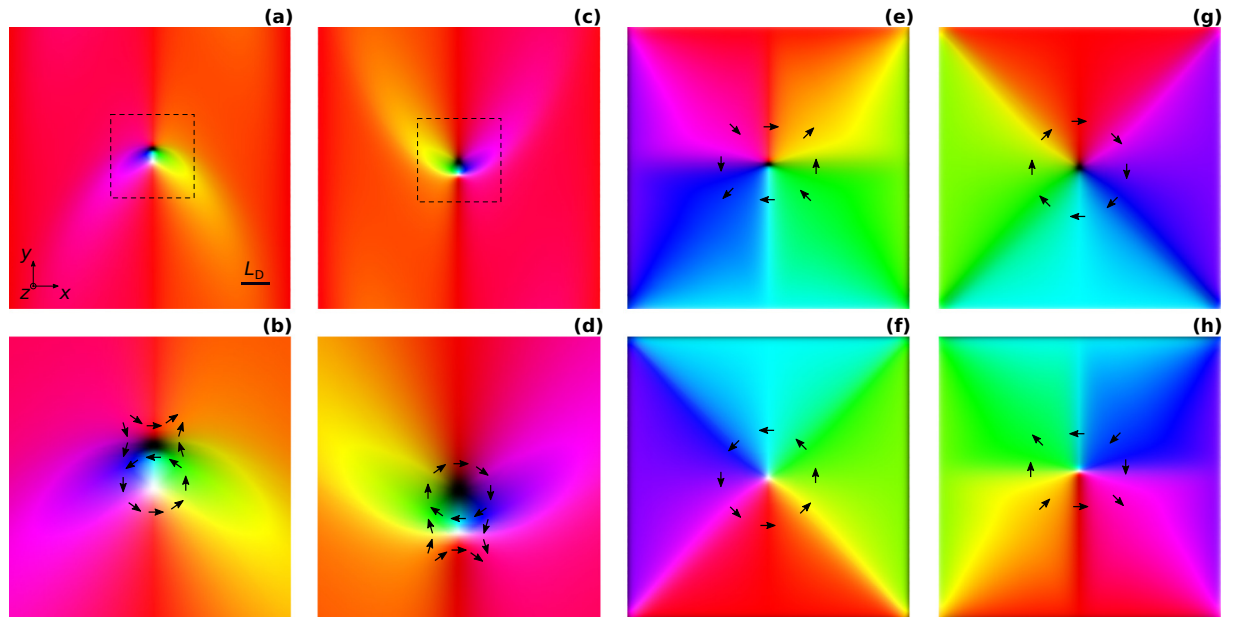


FIG. 6. The equilibrium spin textures obtained by direct energy minimization of functional (1) in the main text for the case of zero external field $h = 0$ and strong easy-plane anisotropy $u = -2$. We use the parameters corresponding to $\Delta l = 52$ and a domain size of $\approx 10L_D \times 10L_D$ [see the scale bar in (a)]. The pairs of vortices and antivortices with a total topological charge, $Q = -1$ in (a) and $Q = +1$ in (c). The zoomed areas indicated by the dashed square in (a) and (c) are shown in (b) and (d), respectively. The pairs of vortices and antivortices in (a) and (c) are calculated with periodical boundary conditions in the xy plane. (e)–(h) show isolated vortices and antivortices with different polarity p and vorticity v : (e) $p = -1$, $v = -1$; (f) $p = 1$, $v = 1$; (g) $p = -1$, $v = 1$; and (h) $p = 1$, $v = -1$. Black arrows indicate the in-plane magnetization.

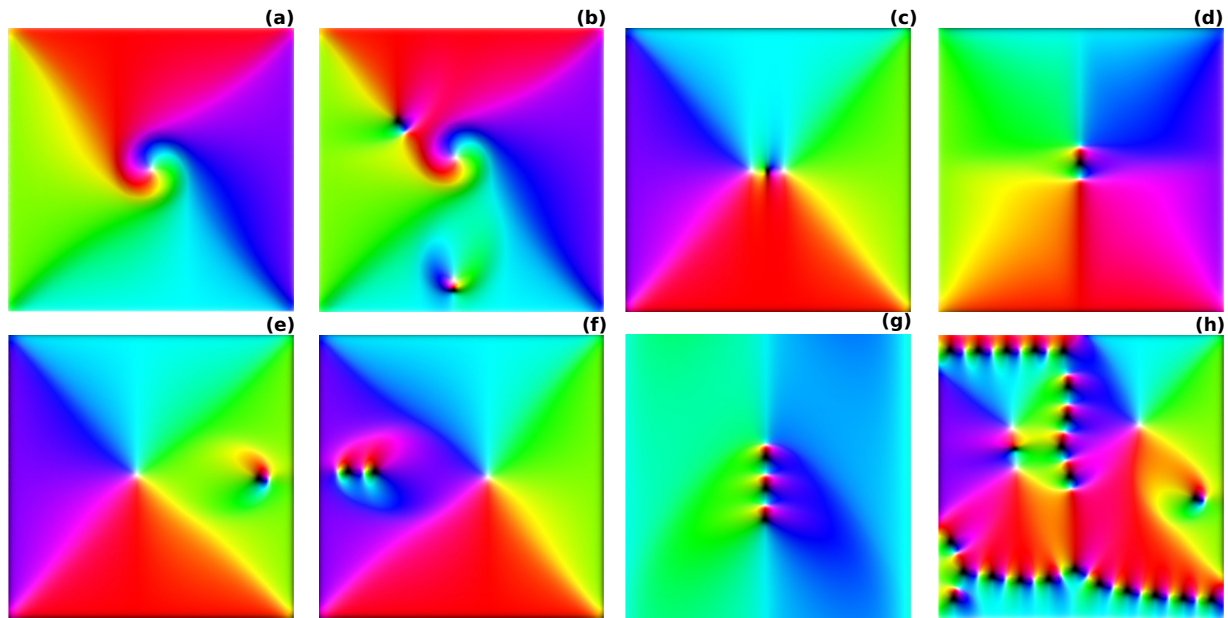


FIG. 7. Various stable spin configurations in the square shape domain with open boundary conditions obtained by energy minimization with the same parameters as in Fig. 6. (a) A vortex with $p = 1$, $\nu = 1$: The same as in Fig. 6(f) but with other types of modulations at the edges. (b) The same vortex as in (a) coexisting with two different vortex-antivortex pairs. (c) A triplet state composed of two vortices and one antivortex. (d) A triplet state composed of two antivortices and one vortex. (e) An example of a state composed of three different types of vortices, where a mutually attractive vortex and antivortex form a localized pair on the right with a topological charge of the pair $Q = +1$. The vortex on the left is repelled by that pair. (f) Another example of the state composed of three different types of vortices. Two vortices and two antivortices form a chain on the left with topological charge $Q = -2$. (g) A chain of alternating vortices and antivortices. (h) An example of a complex state obtained after full energy minimization starting from a random spin distribution. The state contains all four types of vortices and antivortices [see Figs. 6(e)–6(h)]. The state composed of one isolated vortex in the top right quadrant, pairs, triplets, and chains of vortices and antivortices.

decomposed into pair of antivortices in Fig. 6(e) [Fig. 6(h)] and vortices in [Fig. 6(f) [Fig. 6(g)]. Note that due to the presence of DMI the vortex state in Figs. 6(f) and 6(g) have a lower energy than that of antivortices in Figs. 6(e) and 6(h). Isolated vortices are also more stable than the antivortices which are illustrated in Fig. 7(a), where the vortex state remains stable even in the case of unfavorable edge modulations. In contrast to this, the antivortices are unstable at these conditions. For the range of the uniaxial anisotropy value $u > -0.5$ discussed in the main text, the vortices shown in Figs. 6(e)–6(h) are unstable in the whole field range. In other words, at these conditions, the skyrmion is a single object which cannot be decomposed into more elementary particles.

Beside the stability of isolated vortices in the case of strong easy-plane anisotropy, the vortices and antivortices may also form more complex textures (see Fig. 7). In particular, vortices can appear not only in the form of isolated vortices and pairs as in Figs. 7(a) and 7(b), but also can be stable as a triplet state, quadruplet state, etc. Figures 7(c) and 7(d) illustrate some stable triplet states. Note, the vortex-antivortex triplets may appear as a localized bound state only when composed of two types of mutually attracting objects. Only the objects with opposite polarity and opposite vorticity exhibit attractive

interactions. Thereby, only vortices and antivortices can attract each other and only when their polarities are opposite [see Figs. 6(f) and 6(e) for such a vortex and antivortex pair, respectively, and Figs. 6(g) and 6(h) for another pair of the vortices and antivortices]. The interaction of vortices and antivortices with identical polarity always leads to their annihilation. A pair of vortices and a pair of antivortices with opposite polarities are always characterized by repulsion. Figure 7(e) illustrates the state composed of three types of objects with a different character of the interactions: a vortex with positive polarity, a vortex with negative polarity, and an antivortex with positive polarity. The vortex-antivortex coupled pair on the right side of the figure and the vortex on the left side repel each other. A similar configuration with a larger number of vortices and antivortices is shown in Fig. 7(f).

A typical spin texture after full energy minimization from a random distribution is shown in Fig. 7(h). Remarkably, all four types of vortices depicted in Figs. 6(e)–6(h) are present in Fig. 7(h). One may conclude that such configurations can be quantified only by the number of vortices and antivortices. Thereby, in the case of strong easy-plane anisotropy, these four types of vortices and antivortices are the countable objects that describe the state of the system.

[1] A. N. Bogdanov and D. A. Yablonskii, *Sov. Phys. JETP* **68**, 101 (1989).

[2] I. Dzyaloshinsky, *J. Phys. Chem. Solids* **4**, 241 (1958).

[3] T. Moriya, *Phys. Rev.* **120**, 91 (1960).

- [4] F. J. A. den Broeder, W. Hoving, and P. J. H. Bloemen, *J. Magn. Magn. Mater.* **93**, 562 (1991).
- [5] I. Kezsmarki, S. Bordacs, P. Milde, E. Neuber, L. M. Eng, J. S. White, H. M. Ronnow, C. D. Dewhurst, M. Mochizuki, K. Yanai, H. Nakamura, D. Ehlers, V. Tsurkan, and A. Loidl, *Nat. Mater.* **14**, 1116 (2015).
- [6] B. A. Ivanov, V. A. Stephanovich, and A. A. Zhmudskii, *J. Magn. Magn. Mater.* **88**, 116 (1990).
- [7] A. Bogdanov and A. Hubert, *Phys. Status Solidi B* **186**, 527 (1994).
- [8] A. Bogdanov and A. Hubert, *J. Magn. Magn. Mater.* **138**, 255 (1994).
- [9] A. Bogdanov, *JETP Lett.* **62**, 247 (1995).
- [10] A. Bogdanov and A. Hubert, *J. Magn. Magn. Mater.* **195**, 182 (1999).
- [11] C. Melcher, *Proc. R. Soc. A* **470** (2014).
- [12] L. Döring and C. Melcher, *Calc. Var.* **56**, 60 (2017).
- [13] W. Wang, M. Beg, B. Zhang, W. Kuch, and H. Fangohr, *Phys. Rev. B* **92**, 020403(R) (2015).
- [14] M. Ikka, A. Takeuchi, and M. Mochizuki, *Phys. Rev. B* **98**, 184428 (2018).
- [15] T. Koide, A. Takeuchi, and M. Mochizuki, *Phys. Rev. B* **100**, 014408 (2019).
- [16] A. Miyata, O. Portugall, D. Nakamura, K. Ohgushi, and S. Takeyama, *Phys. Rev. B* **96**, 180401(R) (2017).
- [17] C. Wang, H. Du, X. Zhao, C. Jin, M. Tian, Y. Zhang, and R. Che, *Nano Lett.* **17**, 2921 (2017).
- [18] L. Schmidt, J. Hagemeyer, P.-J. Hsu, A. Kubetzka, K. von Bergmann, and R. Wiesendanger, *New J. Phys.* **18**, 099602 (2016).
- [19] A. O. Leonov and I. Kezsmarki, *Phys. Rev. B* **96**, 214413 (2017).
- [20] S. Zhang, J. Zhang, Y. Wen, E. M. Chudnovsky, and X. Zhang, *Commun. Phys.* **1**, 36 (2018).
- [21] T. Suzuki and S.-I. Suga, *Phys. Rev. B* **98**, 180406(R) (2018).
- [22] N. Romming, C. Hanneken, M. Menzel, J. E. Bickel, B. Wolter, K. von Bergmann, A. Kubetzka, and R. Wiesendanger, *Science* **341**, 636 (2013).
- [23] N. Romming, A. Kubetzka, C. Hanneken, K. von Bergmann, and R. Wiesendanger, *Phys. Rev. Lett.* **114**, 177203 (2015).
- [24] X. Z. Yu, Y. Onose, N. Kanazawa, J. H. Park, J. H. Han, Y. Matsui, N. Nagaosa, and Y. Tokura, *Nature (London)* **465**, 901 (2010).
- [25] X. Z. Yu, N. Kanazawa, Y. Onose, K. Kimoto, W. Z. Zhang, S. Ishiwata, Y. Matsui, and Y. Tokura, *Nat. Mater.* **10**, 106 (2011).
- [26] X. Yu, A. Kikkawa, D. Morikawa, K. Shibata, Y. Tokunaga, Y. Taguchi, and Y. Tokura, *Phys. Rev. B* **91**, 054411 (2015).
- [27] A. K. Nayak, V. Kumar, T. Ma, P. Werner, E. Pippel, R. Sahoo, F. Damay, U. K. Rößler, C. Felser, and S. S. P. Parkin, *Nature (London)* **548**, 561 (2017).
- [28] I. E. Dzyaloshinskii, *Sov. Phys. JETP* **20**, 665 (1965).
- [29] U. K. Rößler, A. A. Leonov, and A. N. Bogdanov, *J. Phys.: Conf. Ser.* **303**, 012105 (2011).
- [30] F. N. Rybakov, A. B. Borisov, S. Blügel, and N. S. Kiselev, *Phys. Rev. Lett.* **115**, 117201 (2015).
- [31] F. N. Rybakov and N. S. Kiselev, *Phys. Rev. B* **99**, 064437 (2019).
- [32] The streamlines are a family of curves for which the tangent to the curve at each point of that curve coincides with the direction of the in-plane component of magnetization at this point.
- [33] The polarity of a skyrmion is defined by the direction of magnetization in the center of the skyrmion \mathbf{r}_0 : $p = 1$ for $\mathbf{n}(\mathbf{r}_0) \uparrow \uparrow \hat{e}_z$ and $p = -1$ for $\mathbf{n}(\mathbf{r}_0) \downarrow \downarrow \hat{e}_z$. The vorticity of the skyrmion ν representing an integer number is defined by the line integral along an arbitrary closed path around the center of the skyrmion, $\oint \nabla \Phi(\mathbf{r}) d\mathbf{r} = 2\pi\nu$, where Φ is the azimuthal angle of magnetization at the point \mathbf{r} .
- [34] See Supplemental Material at <http://link.aps.org/supplemental/10.1103/PhysRevB.101.064408> for two video files showing the process of skyrmion fusion.
- [35] J. H. Han, J. Zang, Z. Yang, J.-H. Park, and N. Nagaosa, *Phys. Rev. B* **82**, 094429 (2010).
- [36] N. Nagaosa and Y. Tokura, *Nat. Nanotechnol.* **8**, 899 (2016).
- [37] A. Soumyanarayanan, N. Reyren, A. Fert, and C. Panagopoulos, *Nature (London)* **539**, 509 (2016).
- [38] A. Fert, N. Reyren, and V. Cros, *Nat. Rev. Mater.* **2**, 17031 (2017).
- [39] B. Barton-Singer, C. Ross, and B. J. Schroers, *Commun. Math. Phys.* **1** (2020), doi: 10.1007/s00220-019-03676-1.
- [40] X. Zhang, M. Ezawa, and Y. Zhou, *Sci. Rep.* **5**, 9400 (2015).
- [41] K.-W. Moon, J. Yoon, C. Kim, and C. Hwang, *Phys. Rev. Appl.* **12**, 064054 (2019).
- [42] R. Zarzuela, V. K. Bharadwaj, K.-W. Kim, J. Sinova, and K. Everschor-Sitte, *arXiv:1910.00987*.
- [43] S. D. Yi, S. Onoda, N. Nagaosa, and J. H. Han, *Phys. Rev. B* **80**, 054416 (2009).
- [44] S. Buhrandt and L. Fritz, *Phys. Rev. B* **88**, 195137 (2013).
- [45] V. P. Voronov, B. A. Ivanov, and A. M. Kosevich, *Sov. Phys. JETP* **57**, 1303 (1983).
- [46] A. N. Bogdanov, A. V. Kudinov, and D. A. Yablonskii, *Sov. Phys. Solid State* **31**, 1707 (1989).